Monthly Notices
of the
ROYAL ASTRONOMICAL SOCIETY

MNRAS **489,** 1950–1956 (2019)
Advance Access publication 2019 August 16

doi:10.1093/mnras/stz2258

# Constraining primordial non-Gaussianity using two galaxy surveys and CMB lensing

Mario Ballardini [1,2★] William L. Matthewson[1] and Roy Maartens[1,3]

[1] *Department of Physics & Astronomy, University of the Western Cape, Cape Town 7535, South Africa*
[2] *INAF/OAS Bologna, via Gobetti 101, I-40129 Bologna, Italy*
[3] *Institute of Cosmology & Gravitation, University of Portsmouth, Portsmouth PO1 3FX, UK*

Accepted 2019 August 13. Received 2019 August 5; in original form 2019 July 8

## ABSTRACT

Next-generation galaxy surveys will be able to measure perturbations on scales beyond the equality scale. On these ultra-large scales, primordial non-Gaussianity leaves signatures that can shed light on the mechanism by which perturbations in the early Universe are generated. We perform a forecast analysis for constraining local type non-Gaussianity and its two-parameter extension with a simple scale-dependence. We combine different clustering measurements from future galaxy surveys – a 21cm intensity mapping survey and two photometric galaxy surveys – via the multitracer approach. Furthermore we then include cosmic microwave background (CMB) lensing from a CMB Stage 4 experiment in the multitracer, which can improve the constraints on bias parameters. We forecast $\sigma(f_{\rm NL}) \simeq 0.9$ (1.4) by combining SKA1, a Euclid-like (LSST-like) survey, and CMB Stage 4 lensing. With CMB lensing, the precision on $f_{\rm NL}$ improves by up to a factor of 2, showing that a joint analysis is important. In the case with running of $f_{\rm NL}$, our results show that the combination of upcoming cosmological surveys could achieve $\sigma(n_{\rm NL}) \simeq 0.12$ (0.22) on the running index.

**Key words:** cosmological parameters – early Universe – large-scale structure of Universe.

## 1 INTRODUCTION

The coherent nature of the cosmic microwave background (CMB) anisotropies and the large-scale structure (LSS) we observe around us suggests that the seed for these fluctuations were created at very early times, possibly during a period of inflation (Starobinsky 1980; Guth 1981; Mukhanov & Chibisov 1981; Sato 1981; Albrecht & Steinhardt 1982; Hawking, Moss & Stewart 1982; Linde 1982; Linde 1983)

Inflation observables are predicted to be proportional to the slow-roll parameters for the single field slow-roll (SFSR) models and to be connected through consistency relations for this simplest class of models. For this reason, in the absence of any salient features in the primordial power spectrum, which might open a new observational window on high-energy physics happening in the early Universe (Chen, Namjoo & Wang 2015), SFSR constraints in the next decade will likely be limited to improvements to the constraints on the scalar spectral index and the tensor-to-scalar ratio. The prospects of detecting the running of the scalar spectral index, that arises in SFSR models at second order in slow-roll parameters ($\mathrm{d}n_{\rm s}/\mathrm{dln}\,k \propto (n_{\rm s}-1)^2$), may be nearly impossible even with next-generation cosmological surveys (Ballardini et al. 2016; Muñoz et al. 2017; Li et al. 2018; Mifsud & van de Bruck 2019).

One additional observational probe that allows us access to early-Universe physics is primordial non-Gaussianity (PNG) (see Bartolo et al. 2004; Chen 2010, for reviews). The PNG parameter $f_{\rm NL}$ is predicted to be first order in slow-roll from consistency relations for SFSR model, $f_{\rm NL} \simeq -5(n_{\rm s}-1)/12$ (Acquaviva et al. 2003; Maldacena 2003; Creminelli & Zaldarriaga 2004). On the other hand, an $f_{\rm NL} \gtrsim 1$ is expected for many multifield inflation models (see Byrnes & Choi 2010, for a review).

At present, the best constraints on PNG come from *Planck* measurements of the three-point correlation function of the CMB temperature and polarization anisotropies (Akrami et al. 2019), but LSS is emerging as a promising complementary observable. Non-linear mode coupling from local PNG induces a modulation of the local short-scale power spectrum through a scale-dependence in the bias produced by the long-wavelength primordial gravitational potential $\Phi$ (Salopek & Bond 1990; Gangui et al. 1994)

$$\Phi(\boldsymbol{x}) = \phi(\boldsymbol{x}) + f_{\rm NL}\left(\phi^2(\boldsymbol{x}) - \langle\phi^2\rangle\right) + \mathcal{O}\left(\phi^3\right), \tag{1}$$

where $\phi$ is a Gaussian field. The appearance of $\Phi$ in the halo bias implies a specific form of scale-dependence that cannot be created dynamically (i.e. by late time processes).

This is the main reason that halo bias is such a robust probe of the initial conditions and this gives us the opportunity to study PNG

★ E-mail: mario.ballardini@inaf.it

with two-point statistics of the LSS. Crucially, the $k^{-2}$ scaling which arises for some *local* model of PNG makes the signal largest on the very largest scales of the matter power spectrum (Dalal et al. 2008; Matarrese & Verde 2008; Slosar et al. 2008; Desjacques, Seljak & Iliev 2009; Camera et al. 2013). Such large scales, greater than the equality scale, are affected strongly by cosmic variance, which puts a fundamental limit on the precision with which $f_{\rm NL}$ can be measured (Alonso et al. 2015).

A novel proposal to improve the expected constraints on the amplitude of the PNG fluctuations is to combine the information coming from different LSS tracers or to split the sample in bins of different halo mass in order to reduce the sample variance (Seljak 2009; Yoo et al. 2012; Abramo & Leonard 2013; Ferramacho et al. 2014; Yamauchi, Takahashi & Oguri 2014; Alonso & Ferreira 2015; Ferraro & Smith 2015; Fonseca et al. 2015; Abramo & Bertacca 2017; de Putter & Doré 2017; Fonseca, Maartens & Santos 2017; Fonseca, Maartens & Santos 2018). This is the so-called *multitracer* approach. Moreover, the cross-correlation between clustering and CMB lensing has recently been shown to be particularly well suited to measure local PNG using the scale-dependent halo bias (Giusarma et al. 2018; Schmittfull & Seljak 2018). The cross-correlation between CMB lensing and clustering has a high signal-to-noise ratio and decreases the total effective variance compared to the case considering the two fields independently.

Currently, the tightest constraints on local type PNG are $f_{\rm NL} = -0.9 \pm 5.1$ at 68 per cent CL from the *Planck* 2018 data (Akrami et al. 2019), and $-51 < f_{\rm NL} < 21$ at 95 per cent CL from eBOSS DR14 data (Castorina et al. 2019).

This paper aims to assess the constraining power achievable by a multitracer combination of two next-generation galaxy surveys and a CMB Stage 4 (CMB-S4) survey.

We consider also a generalization of the $f_{\rm NL}$-model (1), in which the parameter $f_{\rm NL}$ is promoted to a function of scale $k$ (Chen 2005; Byrnes, Choi & Hall 2009; Byrnes et al. 2010; Raccanelli, Dore & Dalal 2015)

$$f_{\rm NL}(k) = f_{\rm NL}\left(\frac{k}{k_{\rm piv}}\right)^{n_{\rm NL}}, \tag{2}$$

where $k_{\rm piv}$ is some pivot scale fixed at 0.035 h Mpc$^{-1}$. The tightest current observational constraint on the running index is from the bispectra of the CMB fluctuations: $-0.6 < n_{\rm NL} < 1.4$ at 68 per cent CL from WMAP9 data, for the single-field curvaton scenario (LoVerde et al. 2008; Sefusatti et al. 2009; Becker & Huterer 2012; Oppizzi et al. 2018).

This paper is organized as follows: in Section 2 we describe how the different PNG templates enter into the halo bias through a scale-dependent contribution. We then describe the cosmological surveys considered in our analysis: CMB-S4 as a CMB experiment, SKA1-MID Band 1 IM, and as LSS experiments: Euclid-like and LSST-like. in Section 3. We also introduce the Fisher forecasting formalism in Section 3. Finally, we present our results in Section 4 and we draw our conclusion in Section 5.

## 2 PRIMORDIAL NON-GAUSSIANITY AND LARGE-SCALE STRUCTURE

In this section we describe the large-scale halo bias in the context of the peak-background split (PBS) (Mo & White 1996; Sheth & Tormen 1999; Schmidt & Kamionkowski 2010; Desjacques, Jeong & Schmidt 2018). The PBS method is used to predict the large-scale clustering statistics of dark matter haloes. The Gaussian field is split into long- and short-scale modes $\phi = \phi_\ell + \phi_{\rm s}$, where the long scales determine the clustering of haloes relevant for large-scale power spectrum analysis, while the short scales govern the halo formation.

In order to connect the comoving matter density contrast $\delta$ to the gravitational potential $\Phi$, we make use of the Poisson equation at late times

$$\nabla^2\Phi = -\frac{3}{2}\Omega_{\rm m,0}H_0^2\frac{\delta}{a}, \tag{3}$$

where the potential has been defined under the following convention for the perturbed metric in the Newtonian gauge

$$a^{-2}{\rm d}s^2 = (1+2\Psi){\rm d}\eta^2 - (1-2\Phi){\rm d}x_i{\rm d}x^i\,. \tag{4}$$

At late times the gravitational potential $\Phi$ can be connected to the primordial potential $\Phi_{\rm p}$ by

$$\Phi(\boldsymbol{k},z) = \frac{T(k)\Phi_{\rm p}(\boldsymbol{k})D(z)}{a(z)} \tag{5}$$

where $T(k)$ is the matter transfer function normalized to one at ultra-large scales, and $D(z)$ is the growth factor normalized to the scale factor in the matter-dominated era.

From the Poisson equation (3), we can write the matter density contrast as

$$\delta(\boldsymbol{k},z) = \alpha(k,z)\Phi_{\rm p}(\boldsymbol{k}) \tag{6}$$

with

$$\alpha(k,z) \equiv \frac{2k^2T(k)D(z)}{3\Omega_{\rm m,0}H_0^2}\,. \tag{7}$$

In the presence of local PNG of the form equation (1), the Laplacian of the primordial potential is

$$\nabla^2\Phi_{\rm p} \simeq \nabla^2\phi + 2f_{\rm NL}\left(\phi\nabla^2\phi + |\nabla\phi|^2\right) \tag{8}$$

and we can split its contribution into long and short wavelengths at leading order as

$$\Phi_{\rm l} \approx \phi_{\rm l}, \tag{9}$$

$$\Phi_{\rm s} \approx \phi_{\rm s}\,(1+2f_{\rm NL}\phi_{\rm l})\,. \tag{10}$$

The long-wavelength overdensity $\delta_{\rm l}$ which describes the clustering properties of the matter distribution is not affected by the presence of PNG

$$\delta_{\rm l}(\boldsymbol{k},z) = \alpha(k,z)\phi_{\rm l}(\boldsymbol{k})\,, \tag{11}$$

while the short-wavelength fluctuations are altered by long wavelengths. At lowest order, neglecting white-noise contributions, we have

$$\delta_{\rm s}(\boldsymbol{k}) = \alpha(k,z)\phi_{\rm s}(\boldsymbol{k})\,(1+2f_{\rm NL}\phi_{\rm l})\,. \tag{12}$$

The local number density of haloes in Lagrangian space is given by

$$n_{\rm h} = \bar{n}_{\rm h}\,(1+b_{\rm L}\delta_{\rm l})\,, \tag{13}$$

where $b_{\rm L}$ is the Lagrangian-space bias and $\delta_{\rm l}$ is again the contribution from the long-wavelength modes in (10) that essentially modulate the mean density of the effective local cosmology. Therefore

$$b_{\rm L} = \frac{{\rm d}\ln n_{\rm h}}{{\rm d}\delta_{\rm l}}\,, \tag{14}$$

and the more usual Eulerian-space bias is given by $b = 1 + b_{\rm L}$.

In the presence of PNG, the local number of haloes does not just depend on the large-scale matter perturbations, but it is also affected by the mode coupling between long and short wavelengths that acts like a local rescaling of the amplitude of (small-scale) matter fluctuations. Taylor expanding at first order in these parameters

$$\begin{aligned} b_{\rm L} &= \frac{{\rm d}\ln n_{\rm h}}{{\rm d}\delta_{\rm l}} \\ &= \frac{\partial \ln n_{\rm h}}{\partial \delta_{\rm l}} + \frac{\partial\,(1+2f_{\rm NL}\phi_{\rm l})}{\partial \phi_{\rm l}} \frac{\partial \phi_{\rm l}}{\partial \delta_{\rm l}} \frac{\partial \ln n_{\rm h}}{\partial\,(1+2f_{\rm NL}\phi_{\rm l})} \\ &= \frac{\partial \ln n_{\rm h}}{\partial \delta_{\rm l}} + \frac{2f_{\rm NL}}{\alpha(k,z)} \frac{\partial \ln n_{\rm h}}{\partial \ln \sigma_8^{\rm loc}} \end{aligned} \tag{15}$$

$$= b_{\rm L}^{\rm Gauss} + \Delta b(k,z), \tag{16}$$

where we parametrize the local amplitude of small-scale fluctuations by $\sigma_8^{\rm loc} = \sigma_8\,(1+2f_{\rm NL}\phi_{\rm l})$, and we introduce the scale-dependent contribution to the large-scale bias as

$$\Delta b(k,z) = f_{\rm NL}\frac{\beta_f}{\alpha(k,z)}\,. \tag{17}$$

Finally, on large scales we can relate the halo density contrast to the linear density field as

$$\delta_{\rm h}(\boldsymbol{k},z) = [b(z) + \Delta b(k,z)]\,\delta(\boldsymbol{k},z), \tag{18}$$

where $b = 1 + b_{\rm L}^{\rm Gauss}$ is the Eulerian-space bias connected to the Gaussian Lagrangian-space bias.

Throughout this paper, we will use the expression $\beta_{\rm f} = 2\delta_{\rm c}(b-1)$, which is exact in a barrier crossing model with barrier height $\delta_{\rm c}$ and is a good ($\approx 10$ per cent accuracy) fit to $N$-body simulations (Dalal et al. 2008; Biagetti et al. 2017). We see that, unlike the Gaussian linear bias $b$, the non-Gaussian linear bias will no longer be scale-independent, correcting $b$ by a factor $\propto f_{\rm NL}/k^2$.

Note that there are two conventions to define $f_{\rm NL}$ in equation (1): the LSS convention, where $\Phi$ is normalized at $z=0$, so that $D(0)=1$, and the CMB convention where $\Phi$ is instead the primordial potential, so that $D(a)=a$ in the matter-dominated era. The relation between the two normalizations is

$$f_{\rm NL}^{\rm LSS} = \frac{D(z=\infty)(1+z)}{D(z=0)} f_{\rm NL}^{\rm CMB}\,. \tag{19}$$

We adopt the CMB convention.

## 3 SET-UP

We describe in this section the specifications for the different cosmological surveys used in the analysis and the details of the Fisher methodology used to infer uncertainties on $f_{\rm NL}$ and $n_{\rm NL}$.

### 3.1 CMB lensing specifications

We work with a possible CMB-S4 configuration assuming a 3 arcmin beam and $\sigma_{\rm T} = \sigma_{\rm P}/\sqrt{2} = 1\,\mu$K arcmin noise (Abazajian et al. 2016). We assume $\ell_{\rm min} = 30$ and a different cut at high-$\ell$ of $\ell_{\rm max}^{\rm T} = 3000$ in temperature and $\ell_{\rm max}^{\rm P} = 5000$ in polarization, with $f_{\rm sky} = 0.4$.

For CMB temperature and polarization angular power spectra, the instrumental noise deconvolved with the instrumental beam is defined by (Knox 1995)

$$\mathcal{N}_\ell^{\rm T,P} = \sigma_{\rm T,P} b_\ell^{-2}\,, \tag{20}$$

where we assume a Gaussian beam

$$b_\ell = \exp\left[-\ell(\ell+1)\frac{\theta_{\rm FWHM}^2}{16\ln 2}\right]\,. \tag{21}$$

For CMB lensing, we assume that the lensing reconstruction can be performed with the minimum variance quadratic estimator on the full sky, combining the TT, EE, BB, TE, TB, and EB estimators, calculated according to Hu & Okamoto (2002) with `quicklens`[1] and applying iterative lensing reconstruction (Hirata & Seljak 2003; Smith et al. 2012). We use the CMB lensing information in the range $30 \le \ell \le 3000$.

Note that hereafter we will refer to the full set of angular power spectra of the CMB anisotropies (i.e. temperature, E-mode polarization, CMB lensing, and their cross-correlations) as simply 'CMB'.

### 3.2 H I intensity mapping specifications

IM surveys measure the total intensity emission in each pixel for given atomic lines with very accurate redshifts, without resolving individual galaxies, which are hosts of the emitting atoms (Battye, Davies & Weller 2004; Chang et al. 2008; Wyithe & Loeb 2008; Bull et al. 2015; Santos et al. 2015; Kovetz et al. 2017). The measured brightness temperature fluctuations are expected to be a biased tracer of the underlying cold dark matter distribution.

We consider neutral hydrogen (H I) 21 cm emission and we use the fitting formulas from Santos et al. (2017) for the H I linear bias:

$$b_{\rm HI}(z) = \frac{b_{\rm HI}(0)}{0.677105}\left[0.66655 + 0.17765\,z + 0.050223\,z^2\right], \tag{22}$$

and for the background H I brightness temperature:

$$\bar{T}_{\rm HI}(z) = 0.055919 + 0.23242\,z - 0.024136\,z^2\ {\rm mK}, \tag{23}$$

where $\Omega_{\rm HI}(0)b_{\rm HI}(0) = 4.3\times10^{-4}$ and $\Omega_{\rm HI}(0) = 4.86\times10^{-4}$.

The noise variance for IM with $N_{\rm dish}$ dishes in single-dish mode in the frequency $i$-channel, assuming scale-independence and no correlation between the noise in different frequency channels, is (Knox 1995; Bull et al. 2015)

$$\sigma_{\rm HI}(\nu_i) = \frac{4\pi\, f_{\rm sky} T_{\rm sys}^2(\nu_i)}{2N_{\rm dish} t_{\rm tot}\Delta\nu}\,, \tag{24}$$

$$T_{\rm sys}(\nu_i) = 25 + 60\left(\frac{300\,{\rm MHz}}{\nu_i}\right)^{2.55}\ {\rm K}\,, \tag{25}$$

where $t_{\rm tot}$ is the total observing time. We also include the instrumental limit in angular resolution, characterized by the telescope beam. We assume the noise deconvolved with a Gaussian beam modelled as

$$\mathcal{N}_\ell^{\rm HI}(\nu_i) = \sigma_{\rm HI} b_\ell^{-2}(\nu_i)\,, \tag{26}$$

where $b_\ell(\nu_i)$ is the contribution of the beam in the frequency $i$-channel given by equation (21) with

$$\theta_{\rm FWHM}(\nu) \approx \frac{c}{\nu D_{\rm dish}}\,. \tag{27}$$

For SKA1-MID, we assume $N_{\rm dish} = 197$, $D_{\rm dish} = 15$ m, $t_{\rm tot} = 10^4$ h observing over 20 000 deg$^2$ in the redshift range $0.35 \le z \le 3.05$ (1050 MHz $\ge \nu \ge$ 350 MHz, Band 1) (Bacon et al. 2018). We divide the redshift range into 27 tomographic bins with width 0.1.

[1] https://github.com/dhanson/quicklens

The cleaning of foregrounds from H I IM effectively removes the largest scales, $\ell_{\rm min} \lesssim 5$ (Cunnington et al. 2019; Witzemann et al. 2019), and we take $\ell_{\rm min} = 5$.

### 3.3 Galaxy survey specifications

We present the details of two future photometric galaxy surveys. For each survey we assume the redshift distribution of sources of the form

$$n_{\rm g}(z) \propto z^{\alpha} \exp\left[-\left(\frac{z}{z_0}\right)^{\beta}\right] \text{gal arcmin}^{-2}\,. \tag{28}$$

The distribution of sources in the $i$-th redshift bin, including photometric uncertainties, following (Ma, Hu & Huterer 2005), is

$$n_{\rm g}^{i}(z) = \int_{z_{\rm ph}^{i}}^{z_{\rm ph}^{i+1}} {\rm d}z_{\rm ph}\, n_{\rm g}(z)\, p(z_{\rm ph}|z)\,, \tag{29}$$

where we adopt a Gaussian distribution for the probability distribution of photometric redshift estimates $z_{\rm ph}$, given true redshifts $z$:

$$p(z_{\rm ph}|z) = \frac{1}{\sqrt{2\pi}\,\sigma_z} \exp\left[-\frac{\left(z - z_{\rm ph}\right)^2}{2\sigma_z^2}\right]. \tag{30}$$

The shot noise for galaxies in the $i$-th redshift bin is the inverse of the angular number density of galaxies:

$$\mathcal{N}_{\ell}^{{\rm g}i} = \left(\int {\rm d}z\; n_{\rm g}^{i}(z)\right)^{-1}. \tag{31}$$

Finally, we impose a cut on small scales assuming that we will be able to reconstruct non-linear scales up to $k_{\rm max} = 0.3\,h\,{\rm Mpc}^{-1}$, which corresponds to a redshift-dependent cut in angular space: $\ell_{\rm max} \simeq \chi(z) k_{\rm max}$.

#### 3.3.1 *Euclid-like survey*

The Euclid satellite is a mission of the ESA Cosmic Vision program that will be launched in 2022 (Laureijs et al. 2011). It will perform both a photometric and spectroscopic survey of galaxies. In this work, we focus only on a Euclid-like photometric survey that will cover $\Omega_{\rm sky} = 15\,000$ deg$^2$ measuring $n_{\rm g} = 30$ sources per arcmin$^2$ over a redshift range $0 < z < 2.5$ (Amendola et al. 2018).

The redshift distribution follows equation (28), with $\alpha = 2$, $\beta = 1.5$, and $z_0 = 0.636$, divided into 10 bins each containing the same number of galaxies (Amendola et al. 2018). The scatter of the photometric redshift estimate with respect to the true redshift value is $\sigma_z = 0.05(1 + z)$. The fiducial model for the linear bias is $b(z) = \sqrt{1+z}$ (Amendola et al. 2018). We assume $\ell_{\rm min} = 10$.

#### 3.3.2 *LSST-like survey*

For LSST clustering measurements, we assume a number density of galaxies of $n_{\rm g} = 48$ sources per arcmin$^2$ observed over a patch $\Omega_{\rm sky} = 13\,800$ deg$^2$ and distributed in redshift according to equation (28), with $\alpha = 2$, $\beta = 0.9$, and $z_0 = 0.28$ (Alonso et al. 2018).

We assume 10 tomographic bins spaced by 0.1 between $0.2 \leq z \leq 1.2$, with photometric redshift uncertainties $\sigma_z = 0.03(1 + z)$, and a fiducial model for the bias given by $b(z) = 0.95/D(z)$ (Alonso et al. 2018). We impose $\ell_{\rm min} = 20$.

### 3.4 Fisher analysis

We use the Fisher matrix to derive forecasted constraints on the cosmological parameters, assuming that the observed fields are Gaussian random distributed (for simplicity we ignore information from higher order statistics).

The Fisher matrix at the power spectrum level is then

$$F_{ij} = f_{\rm sky} \sum_{\ell=\ell_{\rm min}}^{\ell_{\rm max}} \left(\frac{2\ell+1}{2}\right) {\rm tr}\left[\mathbf{C}_{\ell,i}\, \Sigma_{\ell}\, \mathbf{C}_{\ell,j}\, \Sigma_{\ell}\right], \tag{32}$$

where $\mathbf{C}_{\ell}$ is the covariance matrix, $\mathbf{C}_{\ell,i} = \partial \mathbf{C}_{\ell}/\partial\theta_i$ is the derivative with respect to the $i$-th cosmological parameter, and $\Sigma_{\ell} = (\mathbf{C}_{\ell} + \mathbf{N}_{\ell})^{-1}$ is the inverse of the total noise matrix, with $\mathbf{N}_{\ell}$ the diagonal noise matrix. This equation assumes that all experiments observe the same patch of sky. We consider for each experiment its own sky fraction and for the cross-correlations the smallest of the sky fractions.

The angular power spectra are

$$C_{\ell}^{XY}(z_i, z_j) = 4\pi \int \frac{{\rm d}k}{k}\, \mathcal{P}_{\mathcal{R}}(k)\, I_{\ell}^{X}(k, z_i)\, I_{\ell}^{Y}(k, z_j)\,. \tag{33}$$

Here $X, Y = {\rm T, E}, \phi$ for the CMB, and $= \Delta_{\rm g}, \Delta_{\rm H\,I}$ for the galaxy clustering/ IM surveys, where $\Delta_g = \delta_g +$ observational corrections from observing on the past light-cone, and similarly for $\Delta_{\rm H\,I}$ (see Challinor & Lewis 2011; Ballardini & Maartens 2019, for details). $\mathcal{P}_{\mathcal{R}}$ is the dimensionless primordial power spectrum and the large-scale structure kernels are

$$I_{\ell}^{\Delta_{\rm g}}(k, z_i) = \int {\rm d}z\; n_{\rm g}^{i}(z) \Delta_{\ell}^{\rm g}(k, z)\,, \tag{34}$$

$$I_{\ell}^{\Delta_{\rm H\,I}}(k, z_i) = \int {\rm d}z\; W_{\rm th}(z, z_i) \bar{T}_{\rm H\,I}(z) \Delta_{\ell}^{\rm H\,I}(k, z)\,, \tag{35}$$

where $\Delta_{\ell}^{\rm g}$, $\Delta_{\ell}^{\rm H\,I}$ are the angular transfer functions (see Ballardini & Maartens 2019) and $W_{\rm th}(z, z_i)$ is a smoothed top-hat window function for the $i$-th bin. We refer the reader to Hu & White (1997) for the details of the CMB temperature and polarization window functions.

All the angular power spectra have been calculated using a modified version of the publicly available code CAMB[2] (Lewis, Challinor & Lasenby 2000; Challinor & Lewis 2011; Howlett et al. 2012).

## 4 RESULTS

The standard cosmological parameter vector that we use is

$$\theta = \left\{\omega_{\rm b}, \omega_{\rm c}, H_0, \tau, \ln\left(10^{10} A_{\rm s}\right), n_{\rm s}\right\}. \tag{36}$$

In addition, we have the PNG parameters depending on the model studied: $\{f_{\rm NL}\}$ or $\{f_{\rm NL}, n_{\rm NL}\}$. We also include a nuisance parameter for each redshift bin, in each of the LSS surveys, allowing for a free redshift evolution of the clustering bias $b$ or of the combination $\bar{T}_{\rm H\,I} b_{\rm H\,I}$ for IM.

The fiducial cosmology used for the standard cosmological parameters, according to *Planck* 2018 (Aghanim et al. 2018a), is $\omega_{\rm b} = 0.022383$, $\omega_{\rm c} = 0.12011$, $H_0 = 67.32$, $\tau = 0.0543$, $\ln(10^{10} A_{\rm s}) = 3.0448$, $n_{\rm s} = 0.96605$. We assume as fiducial $f_{\rm NL} = 0$ without running and $f_{\rm NL} = -0.9$, $n_{\rm NL} = 0$ for the extended model.

Uncertainties reported in the following subsections have been marginalized over all the six standard cosmological parameters and

[2] https://github.com/cmbant/CAMB

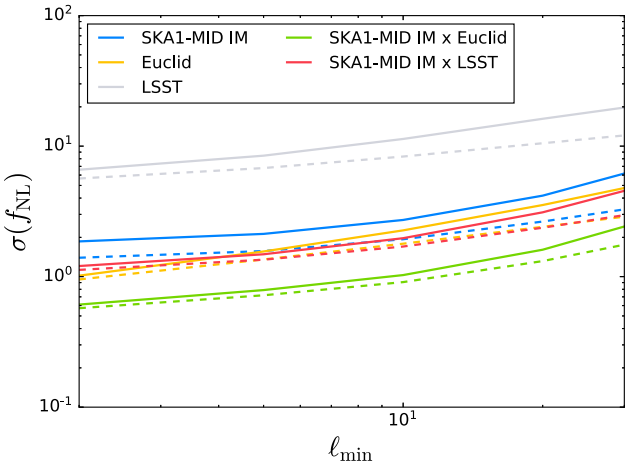


**Figure 1.** Marginalized uncertainties on $f_{\rm NL}$ as function of the minimum multipole $\ell_{\rm min}$ of LSS. Solid curves correspond to LSS experiments without CMB: SKA1 IM (blue), Euclid-like (yellow), LSST-like (grey), and the combinations SKA1 IM × Euclid-like (green) and LSST-like (red). Dashed lines correspond to the inclusion of CMB-S4 lensing ($\ell_{\rm min} = 30$).

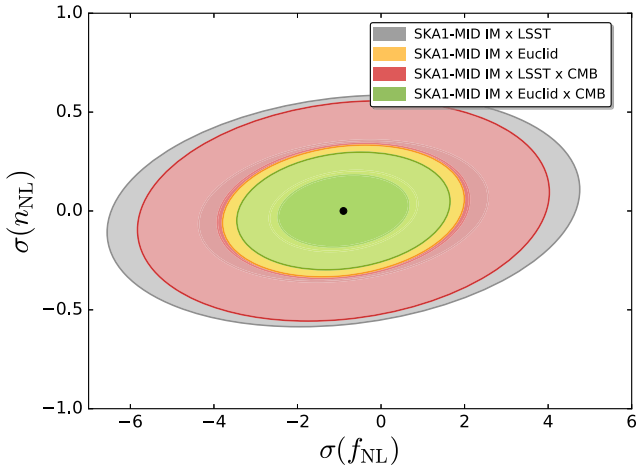


**Figure 2.** Marginalized two-dimensional contours (68 per cent and 95 per cent CL) for $f_{\rm NL}$ and $n_{\rm NL}$, with $\ell_{\rm min} = 5$, 10, 30 for HI IM, galaxy number counts, and CMB respectively. The multitracer combinations are SKA1 × Euclid-like (yellow), SKA1 × LSST-like (grey), CMB × SKA1 × Euclid-like (green), and CMB × SKA1 × LSST-like (red).

the nuisance bias parameters, i.e. 27 temperature-bias parameters for SKA1-HI IM and 10 galaxy bias parameters for Euclid-like/LSST-like.

### 4.1 $f_{\rm NL}$ model of PNG

We consider different minimum multipoles as feasible for the different experimental configurations described in Section 3. In Fig. 1, we present the uncertainties on $f_{\rm NL}$ as a function of $\ell_{\rm min}$.

The uncertainties for single surveys, with the assumed minimum multipole, are

$$\sigma\left(f_{\rm NL}\right) \simeq \begin{cases} 2.1 & \text{SKA1}\ (\ell_{\rm min} = 5)\,, \\ 2.3 & \text{Euclid-like}\ (\ell_{\rm min} = 10)\,, \\ 16.2 & \text{LSST-like}\ (\ell_{\rm min} = 20)\,. \end{cases} \tag{37}$$

Including CMB lensing from CMB-S4 with $\ell_{\rm min} = 30$, using the above $\ell_{\rm min}$ values for LSS and the smallest sky area as the overlap area, the errors in Eq. (37) decrease to

$$\sigma\left(f_{\rm NL}\right) \simeq \begin{cases} 1.6 & \text{SKA1} \times \text{CMB-S4}\,, \\ 1.8 & \text{Euclid-like} \times \text{CMB-S4}\,, \\ 10.5 & \text{LSST-like} \times \text{CMB-S4}\,. \end{cases} \tag{38}$$

The combination of intensity and number counts, using the above $\ell_{\rm min}$ values and the smaller sky area as the overlap area, leads to the errors

$$\sigma\left(f_{\rm NL}\right) \simeq \begin{cases} 0.96 & \text{SKA1} \times \text{Euclid-like}\,, \\ 1.6 & \text{SKA1} \times \text{LSST-like}\,. \end{cases} \tag{39}$$

When all three tracers are combined, the tightest constraints obtained are

$$\sigma\left(f_{\rm NL}\right) \simeq \begin{cases} 0.90 & \text{SKA1} \times \text{Euclid-like} \times \text{CMB-S4}\,, \\ 1.4 & \text{SKA1} \times \text{LSST-like} \times \text{CMB-S4}\,. \end{cases} \tag{40}$$

In addition, we investigate the optimistic case where the minimum multipoles extend down to $\ell_{\rm min} = 2$ for all three tracers. This yields the following constraints for the full multitracer cases

$$\sigma\left(f_{\rm NL}\right) \simeq \begin{cases} 0.47 & \text{SKA1} \times \text{Euclid-like} \times \text{CMB-S4}\,, \\ 1.0 & \text{SKA1} \times \text{LSST-like} \times \text{CMB-S4}\,. \end{cases} \tag{41}$$

### 4.2 $f_{\rm NL}$, $n_{\rm NL}$ model of PNG

We turn now to the constraints for the two-parameter model (2) with a running of $f_{\rm NL}$, using the same specification as in equations (37)–(40). Fig. 2 shows the marginalized uncertainties on the two-dimensional ($f_{\rm NL}$, $n_{\rm NL}$) parameter space.

The uncertainties for single tracers are

$$\sigma\left(n_{\rm NL}\right) \simeq \begin{cases} 2.7 & \text{SKA1}\ (\ell_{\rm min} = 5)\,, \\ 0.35 & \text{Euclid-like}\ (\ell_{\rm min} = 10)\,, \\ 0.37 & \text{LSST-like}\ (\ell_{\rm min} = 20)\,. \end{cases} \tag{42}$$

Including CMB lensing from CMB-S4 with $\ell_{\rm min} = 30$, errors decrease to

$$\sigma\left(n_{\rm NL}\right) \simeq \begin{cases} 1.4 & \text{SKA1} \times \text{CMB-S4}\,, \\ 0.24 & \text{Euclid-like} \times \text{CMB-S4}\,, \\ 0.32 & \text{LSST-like} \times \text{CMB-S4}\,. \end{cases} \tag{43}$$

The combination of intensity and number counts leads to

$$\sigma\left(n_{\rm NL}\right) \simeq \begin{cases} 0.13 & \text{SKA1} \times \text{Euclid-like}\,, \\ 0.24 & \text{SKA1} \times \text{LSST-like}\,. \end{cases} \tag{44}$$

When all three tracers are combined, the tightest constraint obtained is

$$\sigma\left(n_{\rm NL}\right) \simeq \begin{cases} 0.12 & \text{SKA1} \times \text{Euclid-like} \times \text{CMB-S4}\,, \\ 0.22 & \text{SKA1} \times \text{LSST-like} \times \text{CMB-S4}\,. \end{cases} \tag{45}$$

In this case the uncertainties on $f_{\rm NL}$ degrade by $\sim 20$ per cent on average, compared to the case without running, which shows a weak degeneracy between the two parameters.

### 4.3 Comparison with other results on $\sigma(f_{\rm NL})$

In this work, we consistently make use of the CMB convention to define $f_{\rm NL}$. In comparison with other work where the alternative LSS convention is used, we quote here the relevant constraints modified to be consistent with the CMB convention (19).

In Alonso et al. (2015) and Alonso & Ferreira (2015), the case of LSST-like and SKA1-MID IM is treated (without using CMB-S4), giving uncertainties down to ∼0.31 for the multitracer case. They use a greater number of thinner bins for the SKAI-MID IM

survey, i.e. 100 bins with equal co-moving width, while we use 27 such bins. For the LSST-like survey, they use nine bins with widths chosen to ensure equal source density, as opposed to our 10 fixed-width bins. They use a multipole range $2 \leq \ell \leq 500$ for both tracers, and assume larger sky fractions: 0.5 for LSST-like and 0.75 for SKA1, with the overlap taken as 0.4, which also exceeds ours. Their LSST-like redshift distribution has a slightly more pessimistic 40 sources arcmin$^{-2}$, versus our 48 sources arcmin$^{-2}$ according to Alonso et al. (2018), which results in a slightly lower shot noise. In summary, their greater sky area and smaller $\ell_{\rm min}$ are the main reasons for their more optimistic constraints.

In Fonseca et al. (2015) there is a multitracer analysis for Euclid-like and SKA1-MID IM surveys. Their results give $0.72 \leq \sigma(f_{\rm NL}) \leq 1.05$, depending on (a) the maximum multipole chosen ($\ell_{\rm max} = 60$ or $\ell_{\rm max} = 300$), and (b) the sky overlap (50 per cent or 100 per cent). Their multipole range for all tracers extends down to $\ell_{\rm min} = 2$. They also consider a LSST-like survey with sky area equal to that of the entire SKA1-MID IM. They obtain the multitracer result $\sigma(f_{\rm NL}) \simeq 0.61$ for $\ell_{\rm max} = 300$, which is lower than ours. Considering that the effect of $f_{\rm NL}$ is captured only on larger scales, this difference in $\ell_{\rm max}$ should have a negligible effect on the final uncertainties. The sky fraction in their 50 per cent overlap case is 0.18, which is smaller than our shared sky fraction of 0.36 for SKA1-MID IM and Euclid-like. However, their assumed SKA1 sky fraction is 0.72, which is larger than our 0.48, which follows Bacon et al. (2018). Their LSST-like sky fraction is also chosen as 0.72, larger than our sky fraction for LSST-like of $\sim$0.33, according to Alonso et al. (2018). The bias fitting functions used are the same as ours, and the same kind of nuisance parameters are introduced. The main driver of the difference in results from ours is again the greater sky area and smaller $\ell_{\rm min}$ that they assumed.

In Schmittfull & Seljak (2018), the case of LSST-like clustering and CMB-S4 lensing in cross-correlation is investigated. The uncertainties found are $\sigma(f_{\rm NL}) \simeq 0.4$ or $\sigma(f_{\rm NL}) \simeq 1.0$ for the cases where the minimum multipole for both tracers is either 2 or 20. The galaxy redshift distribution is split into six bins, extending over a larger redshift range $0 < z < 7$ and assuming 50 sources arcmin$^{-2}$. The sky fractions they used are 0.5 for both CMB-S4 and LSST-like, assuming 100 per cent overlap. Their fiducial bias model is $b(z) = 1 + z$ as opposed to the one we use, $b(z) = 0.95/D(z)$. Once again, the greater sky area and smaller $\ell_{\rm min}$ that they assumed produce more optimistic constraints than ours. The larger redshift range that they considered is not as important. If we use the assumptions made by them, we recover their results.

## 5 CONCLUSIONS

In this paper we have shown how up to three tracers of the cosmic density field can be used to extract precise measurements of perturbations on scales beyond the equality scale. Specifically we forecast that a conservative combination of an SKA1-MID HI intensity mapping survey with the galaxy clustering from two photometric galaxy surveys (Euclid- and LSST-like), and with CMB lensing from CMB-S4, could reach uncertainties for PNG parameters of $\sigma(f_{\rm NL}) \lesssim 0.9$ and $\sigma(n_{\rm NL}) \lesssim 0.2$. We highlighted the importance of CMB lensing information through the cross-correlation with intensity/number counts to further improve the uncertainties on $f_{\rm NL}$.

The uncertainties obtained for local type PNG in the single-tracer cases are $\sigma(f_{\rm NL}) \simeq 2.1$ for SKA1-MID IM with $\ell_{\rm min} = 5$, $\sigma(f_{\rm NL}) \simeq 2.3$ for Euclid-like with $\ell_{\rm min} = 10$, and $\sigma(f_{\rm NL}) \simeq 16.2$ for LSST-like with $\ell_{\rm min} = 20$. On the running index of $f_{\rm NL}$ in the extended local PNG model, we found $\sigma(n_{\rm NL}) \simeq 2.7, 0.35, 0.37$, respectively.

Combining two different large-scale structure surveys via the multitracer approach, we forecast $\sigma(f_{\rm NL}) \simeq 0.96\,(1.6)$ for SKA1-MID IM with Euclid-like (LSST-like) and $\sigma(n_{\rm NL}) \simeq 0.13\,(0.24)$.

When we combine CMB lensing information (with $\ell_{\rm min} = 30$) from a possible CMB-S4 ground-based experiment in the multitracer, with a single LSS survey, we found that the single-tracer errors decrease to $\sigma(f_{\rm NL}) \simeq 1.6, 1.8, 10.5$ for SKA1-HI IM, Euclid-like, and LSST-like, respectively.

When all three tracers are included in a multitracer analysis, the tightest uncertainties were predicted

$$\sigma(f_{\rm NL}) \simeq 0.90 \text{ and } \sigma(n_{\rm NL}) \simeq 0.12 \quad \text{for SKA1} \times \text{Euclid-like} \times \text{CMB-S4}. \tag{46}$$

Using LSST-like instead of Euclid-like, these degrade to $\sigma(f_{\rm NL}) \simeq 1.4$ and $\sigma(n_{\rm NL}) \simeq 0.22$.

We considered also the possibility of using simulated *Planck*-like data, leading to uncertainties on the cosmological parameters compatible with the latest results in Akrami et al. (2018) and Aghanim et al. (2018a, b) as representative of current CMB measurements. In this case, the improvement in uncertainties by adding *Planck* to the single-tracer cases is very small and mostly due to parameter degeneracy with the standard cosmological parameters, rather than an imprinting of $f_{\rm NL}$ on the cross-correlation between intensity/number counts with CMB lensing. We also tested the possibility of completing the missing first multipoles $2 \leq \ell_{\rm min} < 30$ in the CMB spectra, but we found no further improvement.

Constraints on PNG parameters from the measurement of ultra-large scales depend strongly on the $\ell_{\rm min}$ and $f_{\rm sky}$ considered in the analysis. Our constraints use more conservative estimates and the most up-to-date specifications for the surveys involved. In light of the differences in assumptions made in previous papers, it is not unexpected that our constraints are weaker.

We assumed the minimum multipoles and sky areas for each experiment according to up-to-date specifications for each survey:

$\ell_{\rm min} = 5$, $\Omega = 20\,000$ deg$^2$ – SKA1 (Bacon et al. 2018);

$\ell_{\rm min} = 10$, $\Omega = 15\,000$ deg$^2$ – Euclid-like (Amendola et al. 2018);

$\ell_{\rm min} = 20$, $\Omega = 13\,800$ deg$^2$ – LSST-like (Alonso et al. 2018);

$\ell_{\rm min} = 30$, $\Omega = 16\,500$ deg$^2$ – CMB-S4 (Abazajian et al. 2016).

We also studied how uncertainties change as a function of the minimum multipole, shown in Fig. 1. For the multitracer sky overlap area, we took the smallest of the sky fractions involved. For smaller overlaps, the uncertainties will be mildly negatively affected.

Finally, many other different tracers have been highlighted as good candidates to obtain competitive constraints on $f_{\rm NL}$, such as clusters of galaxies (Pillepich, Porciani & Reiprich 2012; Mana et al. 2013; Sartoris et al. 2016), cosmic infrared background (Tucci, Desjacques & Kunz 2016), cosmic voids (Chan, Hamaus & Biagetti 2019), and different IM lines, like H$\alpha$, CO, and C II (Fonseca et al. 2018; Moradinezhad Dizgah & Keating 2019). These could also be included in the analysis in order to reach more robust and tighter constraints.

## ACKNOWLEDGEMENTS

The authors were supported by the South African Radio Astronomy Observatory, which is a facility of the National Research Foundation, an agency of the Department of Science & Technology. MB was also supported by the Claude Leon Foundation and by ASI

n.I/023/12/0‘Attivitá relative alla fase B2/C per la missione Euclid’. RM was also supported by the UK Science & Technology Facilities Council (Grant no. ST/N000668/1).

## REFERENCES


Abazajian K. N. et al., 2016, preprint (arXiv:1610.02743)
Abramo L. R., Bertacca D., 2017, Phys. Rev., D96, 123535
Abramo L. R., Leonard K. E., 2013, MNRAS, 432, 318
Acquaviva V., Bartolo N., Matarrese S., Riotto A., 2003, Nucl. Phys., B667, 119
Aghanim N. et al., 2018a, preprint (arXiv:1807.06209)
Aghanim N. et al., 2018b, preprint (arXiv:1807.06210)
Akrami Y. et al., 2018, preprint (arXiv:1807.06205)
Akrami Y. et al., 2019, preprint (arXiv:1905.05697)
Albrecht A., Steinhardt P. J., 1982, Phys. Rev. Lett., 48, 1220
Alonso D., Ferreira P. G., 2015, Phys. Rev., D92, 063525
Alonso D., Bull P., Ferreira P. G., Maartens R., Santos M., 2015, ApJ, 814, 145
Alonso D. et al., 2018, preprint (arXiv:1809.01669)
Amendola L. et al., 2018, Living Rev. Rel., 21, 2
Bacon D. J. et al., 2018, preprint (arXiv:1811.02743)
Ballardini M., Maartens R., 2019, MNRAS, 485, 1339
Ballardini M., Finelli F., Fedeli C., Moscardini L., 2016, J. Cosmol. Astropart. Phys., 1610, 041
Bartolo N., Komatsu E., Matarrese S., Riotto A., 2004, Phys. Rep., 402, 103
Battye R. A., Davies R. D., Weller J., 2004, MNRAS, 355, 1339
Becker A., Huterer D., 2012, Phys. Rev. Lett., 109, 121302
Biagetti M., Lazeyras T., Baldauf T., Desjacques V., Schmidt F., 2017, MNRAS, 468, 3277
Bull P., Ferreira P. G., Patel P., Santos M. G., 2015, ApJ, 803, 21
Byrnes C. T., Choi K.-Y., 2010, Adv. Astron., 2010, 724525
Byrnes C. T., Choi K.-Y., Hall L. M. H., 2009, J. Cosmol. Astropart. Phys., 0902, 017
Byrnes C. T., Nurmi S., Tasinato G., Wands D., 2010, J. Cosmol. Astropart. Phys., 1002, 034
Camera S., Santos M. G., Ferreira P. G., Ferramacho L., 2013, Phys. Rev. Lett., 111, 171302
Castorina E. et al., 2019, preprint (arXiv:1904.08859)
Challinor A., Lewis A., 2011, Phys. Rev., D84, 043516
Chan K. C., Hamaus N., Biagetti M., 2019, Phys. Rev., D99, 121304
Chang T.-C., Pen U.-L., Peterson J. B., McDonald P., 2008, Phys. Rev. Lett., 100, 091303
Chen X., 2005, Phys. Rev., D72, 123518
Chen X., 2010, Adv. Astron., 2010, 638979
Chen X., Namjoo M. H., Wang Y., 2015, J. Cosmol. Astropart. Phys., 1502, 027
Creminelli P., Zaldarriaga M., 2004, J. Cosmol. Astropart. Phys., 0410, 006
Cunnington S., Wolz L., Pourtsidou A., Bacon D., 2019
Dalal N., Doré O., Huterer D., Shirokov A., 2008, Phys. Rev., D77, 123514
de Putter R., Doré O., 2017, Phys. Rev., D95, 123513
Desjacques V., Seljak U., Iliev I., 2009, MNRAS, 396, 85
Desjacques V., Jeong D., Schmidt F., 2018, Phys. Rep., 733, 1
Ferramacho L. D., Santos M. G., Jarvis M. J., Camera S., 2014, MNRAS, 442, 2511
Ferraro S., Smith K. M., 2015, Phys. Rev. D, 91, 043506
Fonseca J., Camera S., Santos M., Maartens R., 2015, ApJ, 812, L22
Fonseca J., Maartens R., Santos M. G., 2017, MNRAS, 466, 2780
Fonseca J., Maartens R., Santos M. G., 2018, MNRAS, 479, 3490
Gangui A., Lucchin F., Matarrese S., Mollerach S., 1994, ApJ, 430, 447
Giusarma E., Vagnozzi S., Ho S., Ferraro S., Freese K., Kamen-Rubio R., Luk K.-B., 2018, Phys. Rev., D98, 123526
Guth A. H., 1981, Phys. Rev., D23, 347
Hawking S. W., Moss I. G., Stewart J. M., 1982, Phys. Rev., D26, 2681
Hirata C. M., Seljak U., 2003, Phys. Rev., D68, 083002
Howlett C., Lewis A., Hall A., Challinor A., 2012, J. Cosmol. Astropart. Phys., 1204, 027
Hu W., Okamoto T., 2002, ApJ, 574, 566
Hu W., White M. J., 1997, Phys. Rev., D56, 596
Knox L., 1995, Phys. Rev., D52, 4307
Kovetz E. D. et al., 2017, preprint (arXiv:1709.09066)
Laureijs R. et al., 2011, preprint (arXiv:1110.3193)
Lewis A., Challinor A., Lasenby A., 2000, ApJ, 538, 473
Li X., Weaverdyck N., Adhikari S., Huterer D., Muir J., Wu H.-Y., 2018, ApJ, 862, 137
Linde A. D., 1982, Phys. Lett., 108B, 389
Linde A. D., 1983, Phys. Lett., 129B, 177
LoVerde M., Miller A., Shandera S., Verde L., 2008, J. Cosmol. Astropart. Phys., 0804, 014
Ma Z.-M., Hu W., Huterer D., 2005, ApJ, 636, 21
Maldacena J. M., 2003, JHEP, 05, 013
Mana A., Giannantonio T., Weller J., Hoyle B., Huetsi G., Sartoris B., 2013, MNRAS, 434, 684
Matarrese S., Verde L., 2008, ApJ, 677, L77
Mifsud J., van de Bruck C., 2019, preprint ( arXiv:1904.09590)
Mo H. J., White S. D. M., 1996, MNRAS, 282, 347
Moradinezhad Dizgah A., Keating G. K., 2019, ApJ, 872, 126
Mukhanov V. F., Chibisov G. V., 1981, JETP Lett., 33, 532
Muñoz J. B., Kovetz E. D., Raccanelli A., Kamionkowski M., Silk J., 2017, J. Cosmol. Astropart. Phys., 1705, 032
Oppizzi F., Liguori M., Renzi A., Arroja F., Bartolo N., 2018, J. Cosmol. Astropart. Phys., 1805, 045
Pillepich A., Porciani C., Reiprich T. H., 2012, MNRAS, 422, 44
Raccanelli A., Dore O., Dalal N., 2015, J. Cosmol. Astropart. Phys., 1508, 034
Salopek D. S., Bond J. R., 1990, Phys. Rev., D42, 3936
Santos M. et al., 2015, Proc. Sci., Cosmology from a SKA HI Intensity Mapping Survey. SISSA, Trieste, PoS#19
Santos M. G. et al., 2017, Proceedings, MeerKAT Science: On the Pathway to the SKA (MeerKAT2016): Stellenbosch, South Africa, preprint (arXiv:1709.06099)
Sartoris B. et al., 2016, MNRAS, 459, 1764
Sato K., 1981, MNRAS, 195, 467
Schmidt F., Kamionkowski M., 2010, Phys. Rev., D82, 103002
Schmittfull M., Seljak U., 2018, Phys. Rev., D97, 123540
Sefusatti E., Liguori M., Yadav A. P. S., Jackson M. G., Pajer E., 2009, J. Cosmol. Astropart. Phys., 0912, 022
Seljak U., 2009, Phys. Rev. Lett., 102, 021302
Sheth R. K., Tormen G., 1999, MNRAS, 308, 119
Slosar A., Hirata C., Seljak U., Ho S., Padmanabhan N., 2008, J. Cosmol. Astropart. Phys., 0808, 031
Smith K. M., Hanson D., LoVerde M., Hirata C. M., Zahn O., 2012, J. Cosmol. Astropart. Phys., 1206, 014
Starobinsky A. A., 1980, Phys. Lett., B91, 99
Tucci M., Desjacques V., Kunz M., 2016, MNRAS, 463, 2046
Witzemann A., Alonso D., Fonseca J., Santos M. G., 2019, MNRAS, 485, 5519
Wyithe S., Loeb A., 2008, MNRAS, 383, 606
Yamauchi D., Takahashi K., Oguri M., 2014, Phys. Rev. D, 90, 083520
Yoo J., Hamaus N., Seljak U., Zaldarriaga M., 2012, Phys. Rev., D86, 063514


This paper has been typeset from a TEX/LATEX file prepared by the author.